

# Chemical Science

Accepted Manuscript

This article can be cited before page numbers have been issued, to do this please use: Y. Hasukawa, F. Garcia Escobar, S. Nishimura, K. Takahashi and L. Takahashi, *Chem. Sci.*, 2026, DOI: 10.1039/D6SC00563B.



This is an Accepted Manuscript, which has been through the Royal Society of Chemistry peer review process and has been accepted for publication.

Accepted Manuscripts are published online shortly after acceptance, before technical editing, formatting and proof reading. Using this free service, authors can make their results available to the community, in citable form, before we publish the edited article. We will replace this Accepted Manuscript with the edited and formatted Advance Article as soon as it is available.

You can find more information about Accepted Manuscripts in the [Information for Authors](#).

Please note that technical editing may introduce minor changes to the text and/or graphics, which may alter content. The journal's standard [Terms & Conditions](#) and the [Ethical guidelines](#) still apply. In no event shall the Royal Society of Chemistry be held responsible for any errors or omissions in this Accepted Manuscript or any consequences arising from the use of any information it contains.



## Journal Name

## ARTICLE TYPE

Cite this: DOI: 10.1039/xxxxxxxxxx

# Design Rules for Ternary CO<sub>2</sub> Hydrogenation Catalysts via Literature-Sourced Network Construction and Analysis

Yoshiki Hasukawa<sup>a</sup>, Fernando Garcia-Escobar<sup>a</sup>, Shun Nishimura<sup>b</sup>, Keisuke Takahashi<sup>\*ac</sup> Lauren Takahashi<sup>\*a</sup>

Received Date  
Accepted Date

DOI: 10.1039/xxxxxxxxxx

www.rsc.org/journalname

The development of CO<sub>2</sub> hydrogenation catalysts has largely depended on researchers's trial and error efforts. However, exploring unreported ternary catalysts requires substantial time and cost, highlighting the need for more efficient screening strategies. This study adopts a data-driven informatics approach where literature data is restructured into networks to reveal systematic relationships between reaction conditions and CO<sub>2</sub> conversion. Knowledge extracted from the catalyst combination network further enables the identification of promising ternary catalysts. NiMnPr/Al<sub>2</sub>O<sub>3</sub> and NiMnCe/Al<sub>2</sub>O<sub>3</sub> for CO<sub>2</sub> hydrogenation are rapidly identified and experimentally validated, exhibiting higher CO<sub>2</sub> conversion than their corresponding binary catalysts. Moreover, detailed characterization is carried out for NiMnPr/Al<sub>2</sub>O<sub>3</sub>. These findings and analysis demonstrate that mapping multidimensional data into networks provides a powerful strategy for uncovering correlated variables and facilitating intuitive, highly efficient catalyst development and understanding.

## 1 Introduction

CO<sub>2</sub> hydrogenation, the conversion of carbon dioxide into methane, is a crucial reaction in contexts such as carbon neutrality and space technologies.<sup>1–5</sup> Catalysts centered on Ru and Ni have been explored to date.<sup>6–12</sup> Ru has demonstrated activity at low temperature but is expensive and scarce. Meanwhile, Ni

is inexpensive but faces challenges of exhibiting higher reaction temperature and lower catalytic activity compared with Ru.<sup>13–15</sup> Since Ru-based catalysts are limited by high cost and scarcity, developing Ni-based catalysts with high performance at low temperature is a critical strategy for the practical application of CO<sub>2</sub> hydrogenation.<sup>16,17</sup> In particular, previous catalyst explorations have largely centered on binary catalysts via trial-and-error approaches, whereas ternary catalysts remain unexplored.<sup>18</sup> Given that specific combinations of elements can generate synergistic interactions, in which the catalytic activity deviates from that of the individual components or their simple average, ternary systems hold strong potential.<sup>19</sup> Therefore, the exploration of ternary catalysts are explored as they may realize synergistic performance gains unattainable with binary formulations.

Trial-and-error catalyst development is often inefficient in terms of both cost and time.<sup>20</sup> In contrast, data-driven catalyst informatics can extract hidden trends and patterns from diverse variables in catalysts data, thereby offering opportunities for more efficient and useful catalyst discovery.<sup>21–24</sup> Machine learning has been used to successfully discover previously unreported and potentially promising catalysts.<sup>25,26</sup> However, a major challenge lies in the black-box nature of machine learning, which obscures both the reasoning behind the predictions and the underlying learning process in the dataset.<sup>27</sup> To address this problem, catalyst network analysis utilizing graph theory has emerged. This approach visualizes the relationship between catalytic activity and multidimensional variables, providing human-readable insights.<sup>28–30</sup> Based on the positional relationships within the network, it enables reaction condition optimization, efficient catalyst screening, and catalyst design.

Based on the above context and challenges, multidimensional analysis and ternary catalysts design through catalyst screening are performed for CO<sub>2</sub> hydrogenation dataset. Network construction and analysis is used in order to better understand the relationship between multidimensional factors and CO<sub>2</sub> conversion

<sup>a</sup> Department of Chemistry, Hokkaido University, North 10, West 8, Sapporo 060-0810, Japan

<sup>c</sup> List Sustainable Digital Transformation Catalyst Collaboration Research Platform, Institute for Chemical Reaction Design and Discovery, Hokkaido University, Sapporo 001-0021, Japan

<sup>b</sup> Graduate School of Advanced Science and Technology, Japan Advanced Institute of Science and Technology, 1-1 Asahidai, Nomi, Ishikawa 923-1292, Japan

\* email: keisuke.takahashi@sci.hokudai.ac.jp

\* email: lauren.takahashi@sci.hokudai.ac.jp



and to improve the efficiency of ternary catalyst design from binary catalysts data, thereby providing a means for accelerated catalysts exploration.

## 2 Method

### 2.1 Data Details

A dataset comprising 4051 entries collected from 100 papers is used for the network analysis of catalytic studies.<sup>26</sup> Table 1 summarizes the category of the dataset and their features. After removing entries containing missing values, 3531 entries are employed for network construction.

**Table 1** The features and their explanations in the dataset<sup>26</sup>.

Category	Features
Catalyst information	Base
	Base wt%
	Base 2
	Base 2 wt%
	Support
	Support wt%
Preparation condition	Support 2
	Catalyst preparation method
	Calcination Temperature (°C)
	Calcination time (h)
	Reduction Temperature (°C)
	Reduction Pressure (bar)
	Reduction time (h)
Reduction H <sub>2</sub> %	
Reaction condition	Temperature (°C)
	Pressure (bar)
	W/F (mg <sub>Cat</sub> *mL/min)
	Time on Stream (h)
	CO % in feed
	Inert % in feed
	CH <sub>4</sub> % in feed
	H <sub>2</sub> O % in feed
	H <sub>2</sub> /CO <sub>2</sub> % in feed
	CO <sub>2</sub> Conversion %
Catalyst activity	CO <sub>2</sub> Conversion %

### 2.2 Preprocessing for network construction

To construct the network, the following features are utilized and preprocessed: Base, Base wt%, Base 2, Base 2 wt%, Support, Support wt%, Calcination temperature(°C), Calcination time(h), Temperature(°C), W/F(mg<sub>Cat</sub>\*mL/min), Inert % in feed, and CO<sub>2</sub> conversion %. To better understand the relationship between catalyst information and catalyst activity, Base wt%, Base 2 wt%, Support wt%, and CO<sub>2</sub> conversion% are clustered using the one dimensional K-Means algorithm. The number of clusters for each dataset is decided based on the distribution of each variables. By this algorithm, Base wt% is clustered into 5 bins (0.0-7.0%, 7.5-15.0%, 17.0-26.0%, 27.5-40.0%, 47.0-100.0%), Base 2 wt% into 4 bins(0.0-3.0%, 4.0-10.0%, 12.5-17.0%, 25.0-37.5%), Support wt% into 4 bins(0.0-60.7%, 62.5-80.0%, 81.0-91.5%, 92.0-100.0%), and CO<sub>2</sub> conversion into 10 bins(0.0-5.61%, 5.63%-14.15%, 14.19-24.52%, 24.62-35.37%, 35.4-46.03%, 46.08-56.88%, 57.0-67.53%, 67.59-77.5%, 77.52-

88.38%, 88.41-100.0%).

Two networks, N-1 and N-2, are constructed in this work. For N-1 network, each catalyst element is represented as a node along with its respective content. Here, nodes are defined as vertices which represents Base, Base 2, Support, Calcination temperature, Calcination time, Temperature, W/F, Inert gas, CO<sub>2</sub> conversion. Edges are links that are added between CO<sub>2</sub> conversion and each of the other variables(Base, Base2, Support, Calcination temperature(°C), Calcination time(h), Temperature(°C), W/F, Inert % in feed) when the corresponding pair is observed together within the same record in the dataset. Note that this is purely a visualization outcome of the layout algorithm, and the geometric distances should not be interpreted as precise numerical distances since nodes sharing more edges are placed closer to each other. The layouts of both networks are constructed as undirected graphs via ForceAtlas2 algorithm within Gephi application to visualize the relationship of between CO<sub>2</sub> conversion and other features<sup>31,32</sup>. The edge weight is set to 1. Node size is determined by degree ranking within a range of 10 to 40. Additionally, for visibility purposes, the labels are represented in a simplified manner on the network: Base as b, Base2 as b2, Support as s, Calcination Temperature as cTemp, Calcination time as cTime, Temperature as T, W/F as W/F, Inert in feed as inert, and CO<sub>2</sub> Conversion as conv. For example, one data(Base: Ni, Base wt%: 10.0, Base 2: None, Base 2 wt%: 0.0, Support: Al<sub>2</sub>O<sub>3</sub>, Support: wt%: 90.0, Calcination Temperature (°C): 600, Calcination time (h): 4.0, Temperature(°C): 350, W/F: 5.26, Inert in feed%: 21.0, CO<sub>2</sub> Conversion %: 25.552) of the network N-1 is represented as nodes: b-Ni:7.5-15.0, b2-None, s-Al<sub>2</sub>O<sub>3</sub>:81.0-91.5, cTemp:600, cTime:4.0, temp:350, W/F:5.26, inert:21.0, and conv:24.62-35.37 as shown in Figure S1. In the network N-2, nodes are constructed by combining Base and Base2 to represent the catalyst combinations. For example, one data(Base: Ni, Base wt%: 10.0, Base 2: None, Base 2 wt%: 0.0, Support: Al<sub>2</sub>O<sub>3</sub>, Support: wt%: 90.0, Calcination Temperature (°C): 600, Calcination time (h): 4.0, Temperature(°C): 350, W/F: 5.26, Inert in feed %: 21.0, CO<sub>2</sub> Conversion %: 25.552) is represented as nodes: Ni(7.5-15.0)None(), s-Al<sub>2</sub>O<sub>3</sub>:81.0-91.5, cTemp:600, cTime:4.0, T:350, W/F:5.26, inert:21.0, and conv:24.62-35.37 as shown in Figure S2.

### 2.3 Experimental

#### 2.3.1 Catalyst Preparation

The tested catalysts are prepared by impregnating a support oxide with water-soluble metallic precursors in combinations presented on Table 2.

$\gamma$ -ALUMINA ( $\gamma$ -Al<sub>2</sub>O<sub>3</sub>, KOJUNDO CHEMICAL LABORATORY Co., LTD., 99.0%) is used as support for catalysts. Iron(II) nitrate nonahydrate (Fe(NO<sub>3</sub>)<sub>3</sub> · 9H<sub>2</sub>O, min. 99.0%) from Junsei Chemical CO.Ltd and Nickel (II) Nitrate hexahydrate (Ni(NO<sub>3</sub>)<sub>2</sub> · 6H<sub>2</sub>O, wako special grade), Manganese(II) Acetate Tetrahydrate ((CH<sub>3</sub>COO)<sub>2</sub>Mn, wako special grade), Cerium(II) Nitrate Hexahydrate(Ce(NO<sub>3</sub>)<sub>3</sub> · 6H<sub>2</sub>O, wako special grade), Praseodymium(III) Nitrate n-Hydrate(Pr(NO<sub>3</sub>)<sub>3</sub> · nH<sub>2</sub>O, 99.5%), Barium Acetate (Ba(CH<sub>3</sub>COO)<sub>2</sub>, min. 99.0%), min. 99.0%),



Cobalt(II) Acetate ((CH<sub>3</sub>COO)<sub>2</sub>Co · 4H<sub>2</sub>O, wako special grade), and Sodium Nitrate (NaNO<sub>3</sub>, min. 99.0%) from FUJIFILM Wako Pure Chemical Corporation are used as precursors for the impregnated metals in the catalysts.

All catalysts are synthesized according to the following procedure. 2 g of the support (γ-Al<sub>2</sub>O<sub>3</sub>) are dispersed in 100 mL of pure water under continuous stirring. Separately, the metallic precursors for M1, M2 and M3 are each dissolved in 50 mL of pure water to achieve 5 wt% each in the final catalyst based on the calculated precursor quantities for complete impregnation. The metallic solutions are sequentially added to the support dispersion at 5 minutes intervals in M1-M2-M3 order. After stirring for 1 hour, the dispersion is aged 24 hours without stirring at room temperature. The stirring is restarted and the water is evaporated. The remaining powder is collected and dried at 80 °C for 12 hours. Finally, the material is ground in a mortar, calcined at 500 °C for 3.0 hours and ground again before testing. For comparison, unary and binary catalysts are also prepared by the same procedure.

**Table 2** M1-M2-M3 combinations of the prepared γ-Al<sub>2</sub>O<sub>3</sub>-supported catalysts.

Label	M1	M2	M3
NiMnCe/Al <sub>2</sub> O <sub>3</sub>	Ce	Ni	Mn
NiMnPr/Al <sub>2</sub> O <sub>3</sub>	Pr	Ni	Mn
NiMnBa/Al <sub>2</sub> O <sub>3</sub>	Ba	Mn	Ni
NiMnCo/Al <sub>2</sub> O <sub>3</sub>	Mn	Co	Ni
NiMnNa/Al <sub>2</sub> O <sub>3</sub>	Na	Ni	Mn
NiMnFe/Al <sub>2</sub> O <sub>3</sub>	Mn	Fe	Ni
NiMn/Al <sub>2</sub> O <sub>3</sub>	Mn	Ni	-
NiCe/Al <sub>2</sub> O <sub>3</sub>	Ce	Ni	-
NiPr/Al <sub>2</sub> O <sub>3</sub>	Pr	Ni	-
MnPr/Al <sub>2</sub> O <sub>3</sub>	Pr	Mn	-
Ni/Al <sub>2</sub> O <sub>3</sub>	Ni	-	-
Mn/Al <sub>2</sub> O <sub>3</sub>	Mn	-	-
Pr/Al <sub>2</sub> O <sub>3</sub>	Pr	-	-

### 2.3.2 Catalyst Activity and Characterization

Catalyst performance is tested in fixed-bed quartz reactor (L = 375 mm, ID = 0.75 mm) under ambient pressure. The catalyst powder (100 mg) is placed between two layers of quartz wool. The reactor temperature is monitored using a K-type thermocouple, with the tip placed near the outer reactor wall of the catalyst bed location. Prior to measurement run, the system is purged at 50 °C for 20-30 min. under N<sub>2</sub> gas at a flow of 50 mL/min, then cooled down under a N<sub>2</sub>/H<sub>2</sub>/CO<sub>2</sub> flow of 25/20/5 ml/min. After measuring at room temperature and confirming the absence of impurities in the outlet flow, catalyst performance is studied at 150-450 °C at 50 °C intervals under the same gas flow conditions. The reaction mixture is analyzed by using a Shimadzu GC-2014 chromatograph equipped with a SHINCARBON ST 50/80 mesh column (3 mm x 2 m, He carrier). CO<sub>2</sub> conversion and yield (CO and CH<sub>4</sub>) are estimated using N<sub>2</sub> as an internal standard. CO<sub>2</sub> conversion is calculated in accordance to Equation 1. Product P yield for CO and CH<sub>4</sub> is calculated in accordance to Equation 2,

where  $n = 1$  for CO and CH<sub>4</sub>. To ensure reproducibility, each catalyst is tested twice. The 12 hour durability testing is conducted on NiMnPr/Al<sub>2</sub>O<sub>3</sub> under H<sub>2</sub>/CO<sub>2</sub> of 4 at 450 °C.

$$CO_{2Conv} = \frac{(CO_{2In}/N_{2In}) - (CO_{2Out}/N_{2Out})}{(CO_{2In}/N_{2In})} \times 100 \quad (1)$$

$$P_{Yield} = \frac{n(P_{Out}/N_{2Out})}{(CO_{2In}/N_{2In})} \times 100 \quad (2)$$

$$P_{selectivity} = \frac{P_{yield}}{CO_{2Conv}} \times 100 \quad (3)$$

Scanning electron microscopy (JEOL Neo-Scope JCM-7000), and X-ray diffraction (Rigaku MiniFlex600-C) are used in order to obtain surface condition of samples and crystal structure. XRD is performed to obtain diffraction pattern over the 2θ of 3-90 with a step size 0.01 ° and a scan of 10 ° per /min.

CO<sub>2</sub> uptake is performed to evaluate the CO<sub>2</sub> adsorption-desorption properties. After degassing the samples at 300 °C for 2 h under vacuum to remove adsorbed moisture and surface impurities, CO<sub>2</sub> adsorption-desorption measurements are carried out using a BELSORP MINI X. CO<sub>2</sub> adsorption isotherms are obtained at room temperature (25 °C) by increasing the pressure from 0 to 100 kPa, and desorption are subsequently recorded by decreasing the pressure.

TPR profile is monitored with a TCD detector by BELCAT II system (MicrotracBEL, Co., Osaka, Japan). 50 mg of sample is pretreated under an He flow (30.0 mLmin<sup>-1</sup>) at 500 °C for 1 h, and cooled to 45 °C. H<sub>2</sub>-TPR profile is observed under a 10 vol% H<sub>2</sub>/Ar flow (30.0 mLmin<sup>-1</sup>) from 50 °C to 900 °C at the ramping rate of 10.0 °Cmin<sup>-1</sup>. A molecular sieves 4A trap is placed at the line between an out-let of the sample bed and a TCD detector.

## 3 Result and Discussion

### 3.1 Network Construction and Analysis

The network N-1 is constructed and analyzed to investigate the relationship between CO<sub>2</sub> conversion and other features as shown in Figure 1. Construction of the N-1 network results in an undirected network which has 360 nodes and 28,248 edges. The edge weight is set to 1. Node size is determined by degree ranking within a range of 10 to 40. Node placement is determined by the relationship of a node against all other nodes within the network. As seen in Figure 2, the network structure reveals that nodes for CO<sub>2</sub> conversion are placed in groups that can be interpreted as areas of low, medium, and high CO<sub>2</sub> conversion. The nodes for CO<sub>2</sub> conversion are defined as follows: low conversion: 0.00–5.61 % and 5.63–14.15 %; medium conversion: 35.40–45.03 %, 46.08–56.88 %, and 57.00–67.53 %, as well as 69.59–77.50 %; high conversion: 77.52–88.38 % and 88.41–100 %. By looking at nodes found within each CO<sub>2</sub> conversion area, it becomes possible to understand the factors associated with that range of CO<sub>2</sub> conversion, thereby making it possible to include multidimensionality during analysis.

N-1 is analyzed to investigate the relationship between experiment conditions and CO<sub>2</sub> conversion. Temperature is found to exhibit a pronounced trend with CO<sub>2</sub> conversion as shown in Fig-



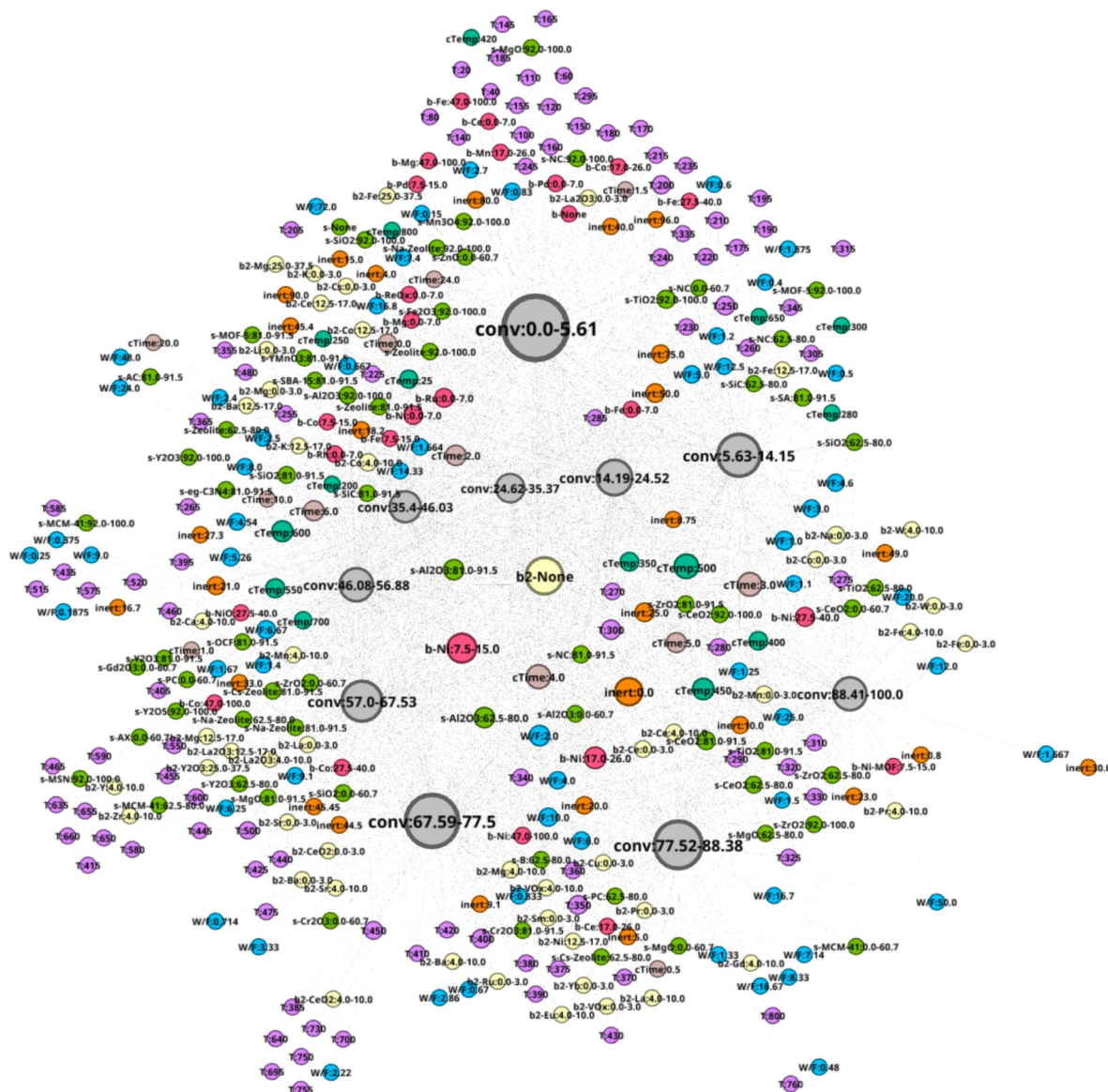


**Fig. 1** The N-1 network. Each variable is color-coded: pink(Base), yellow(Base 2), green(Support), emerald(Calcination temperature( $^{\circ}$ C)), light brown(Calcination time(h)), light purple(Temperature( $^{\circ}$ C)), light blue(W/F(mgcat/minml)), orange(Inert % in feed), and gray( $\text{CO}_2$  conversion, %). Note that labels are adjusted, and node size is determined by degree ranking within a range of 10 to 40 for visualization purposes. A higher resolution of this network can be found in the support information.

Chemical Science Accepted Manuscript



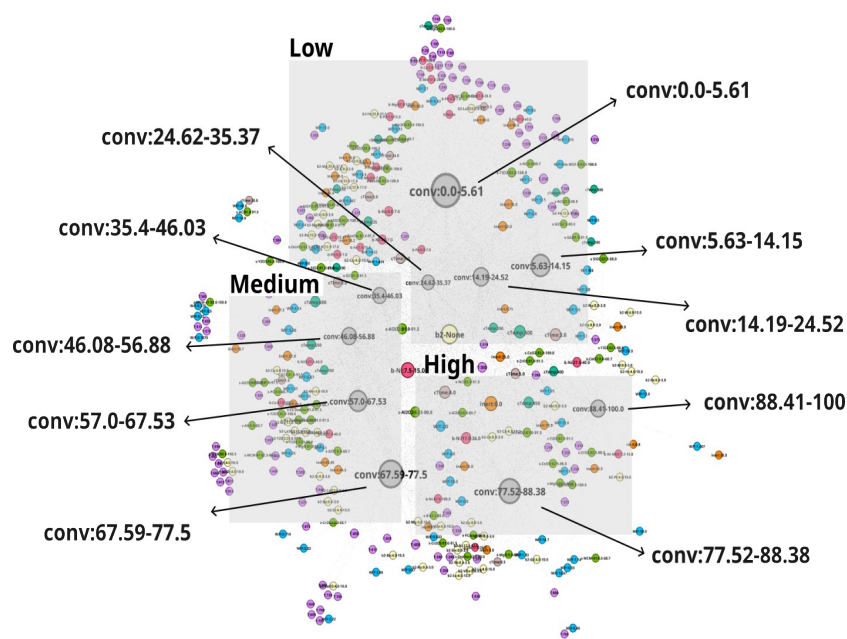


**Fig. 2** A large picture of N-1. Each variable is color-coded: pink(Base), yellow(Base 2), green(Support), emerald(Calcination temperature(°C)), light brown(Calcination time(h)), light purple(Temperature(°C)), light blue(W/F(mgcat/minml)), orange(Inert % in feed), and gray(CO<sub>2</sub> conversion, %). Areas up to 35.37 % is defined as low CO<sub>2</sub> conversion area, 35.4 % to 77.5 % is defined as medium CO<sub>2</sub> conversion area, and greater than 77.52 % is defined as high CO<sub>2</sub> conversion area. A higher resolution of this network can be found in the support information.

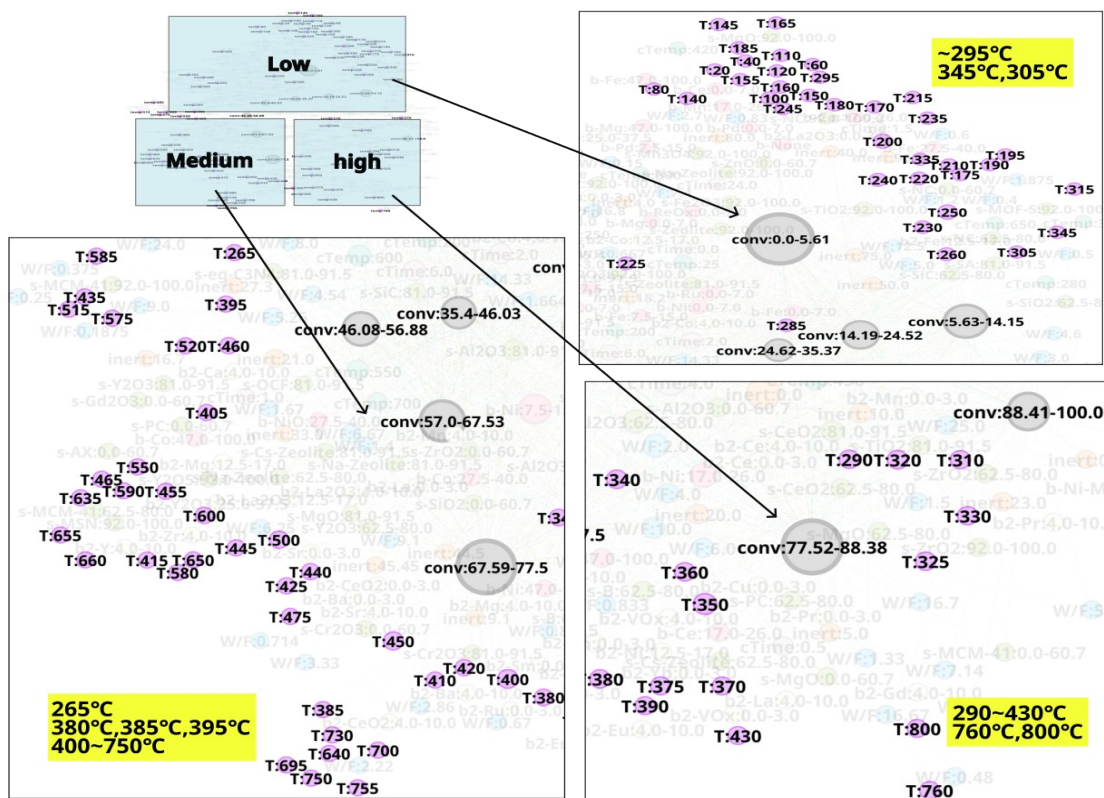


**Fig. 3** Relationship between temperature(°C) and CO<sub>2</sub> conversion(%) based on the N-1 network which shows enlarged views of regions where temperatures are concentrated. Nodes of temperature(light purple) and CO<sub>2</sub> conversion(gray) are highlighted. Areas up to 35.37 % is defined as low CO<sub>2</sub> conversion area, 35.4 % to 77.5 % is defined as medium CO<sub>2</sub> conversion area, and greater than 77.52 % is defined as high CO<sub>2</sub> conversion area. Note that labels are adjusted, and node size is determined by degree ranking within a range of 10 to 40 for visualization purposes. A higher resolution of this network can be found in the support information.



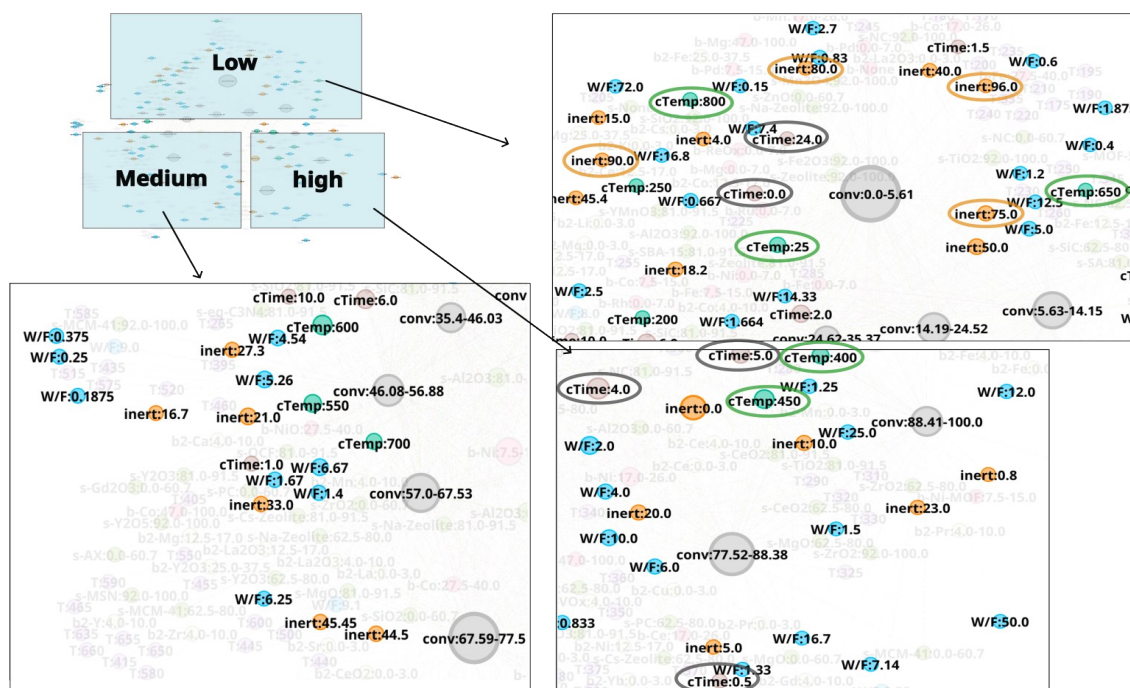


**Fig. 4** Relationship between CO<sub>2</sub> conversion(%) and experimental conditions(W/F, Inert % in feed, inert; Calcination temperature(°C), cTemp; Calcination time(h), cTime) based on the N-1 network. Areas up to 35.37 % is defined as low CO<sub>2</sub> conversion area, 35.4 % to 77.5 % is defined as medium CO<sub>2</sub> conversion area, and greater than 77.52 % is defined as high CO<sub>2</sub> conversion area. Note that labels are adjusted, and node size is determined by degree ranking within a range of 10 to 40 for visualization purposes. A higher resolution of this network can be found in the support information.

ure3. Low temperature range below 200 °C strongly correlates to low CO<sub>2</sub> conversion area. On the other hand, 300-400 °C temperature range is dispersed among low, medium, and high CO<sub>2</sub> conversion area. This suggests that CO<sub>2</sub> conversion may vary significantly depending on the catalyst composition and other experimental conditions within a temperature range of 300-400 °C; in this situation, temperature may have less impact on CO<sub>2</sub> conversion in comparison to other experimental factors. Temperature range of 400-750 °C mainly correlates to medium CO<sub>2</sub> conversion range, whereas 430 °C, 800 °C, and 760 °C is included to the high CO<sub>2</sub> conversion area. The relationship between other variables and CO<sub>2</sub> conversion is shown in Figure4. It can be seen that calcination temperatures (cTemp) of 400 or 450 °C and calcination times (cTime) of 0.5, 4.0, or 5.0 h are associated with high CO<sub>2</sub> conversion, whereas low or high calcination conditions (e.g. 25 °C, 650 °C, or 800 °C and 0 or 24 hours) are included in the area of low CO<sub>2</sub> conversion area. Therefore, intermediate calcination temperatures and times such as 400-450 °C and 4-5hours, rather than low or high calcination temperatures and time, are possibly ideal conditions to consider for catalyst synthesis. As shown in Figure4, nodes with a high inert % in feed(inert) are associated with low CO<sub>2</sub> conversion, thereby showing these conditions are likely to be undesirable for achieving efficient CO<sub>2</sub> conversion. In this way, by converting literature data into a network and focusing on experimental conditions, it becomes possible to identify conditions that are effective for CO<sub>2</sub> conversion as well as those that should be avoided.

The high CO<sub>2</sub> conversion area in the N-1 network is focused to investigate the relationship between catalysts and CO<sub>2</sub> conver-

sion. As shown in Figure 5, Ni, Ce, and Ni-MOF used as “Base 1” exhibit high CO<sub>2</sub> conversion. Na, Co, W, Fe, Mn, Pr, Ce, VO<sub>x</sub>, Cu, Sm, Ni, Yb, La, Eu, Gd and Ru are also included as “Base 2.” Supports include TiO<sub>2</sub>, ZrO<sub>2</sub>, CeO<sub>2</sub>, MgO, MCM-41, B, Cr<sub>2</sub>O<sub>3</sub>, PC, Al<sub>2</sub>O<sub>3</sub> and Cs-Zeolite. Although these elements and supports are correlated with high CO<sub>2</sub> conversion, it is necessary to investigate the relationship between CO<sub>2</sub> conversion and catalyst combinations of Base 1 and Base 2 for a better understanding.

### 3.2 Catalyst Screening

Another network, N-2, is constructed to explore catalyst combinations and screen for promising combinations. The N-2 network is constructed to investigate the relationship between catalyst combinations and CO<sub>2</sub> conversion as shown in Figure6. As shown in Figure S2, Base1 and Base2 are represented as single nodes, and the relationship between element pairs and CO<sub>2</sub> conversion clarifies whether those pairs are effective in improving CO<sub>2</sub> conversion. It results in an undirected network which has 379 nodes and 24,717 edges. The edge weight is set to 1. Node size is determined by degree ranking within a range of 10 to 40. Similarly to the case of the N-1 network, the network structure reveals that nodes for CO<sub>2</sub> conversion are placed in groups that can be interpreted as areas of low, medium, and high CO<sub>2</sub> conversion as shown in Figure7. The nodes for CO<sub>2</sub> conversion are defined as follows: low conversion: 0.00–5.61 % and 5.63–14.15 %; medium conversion: 35.40–45.03 %, 46.08–56.88 %, and 57.00–67.53 %, as well as 69.59–77.50 %; and high conversion: 77.52–88.38 % and 88.41–100 %. By looking at nodes included in each CO<sub>2</sub> conversion area, it becomes possible to understand



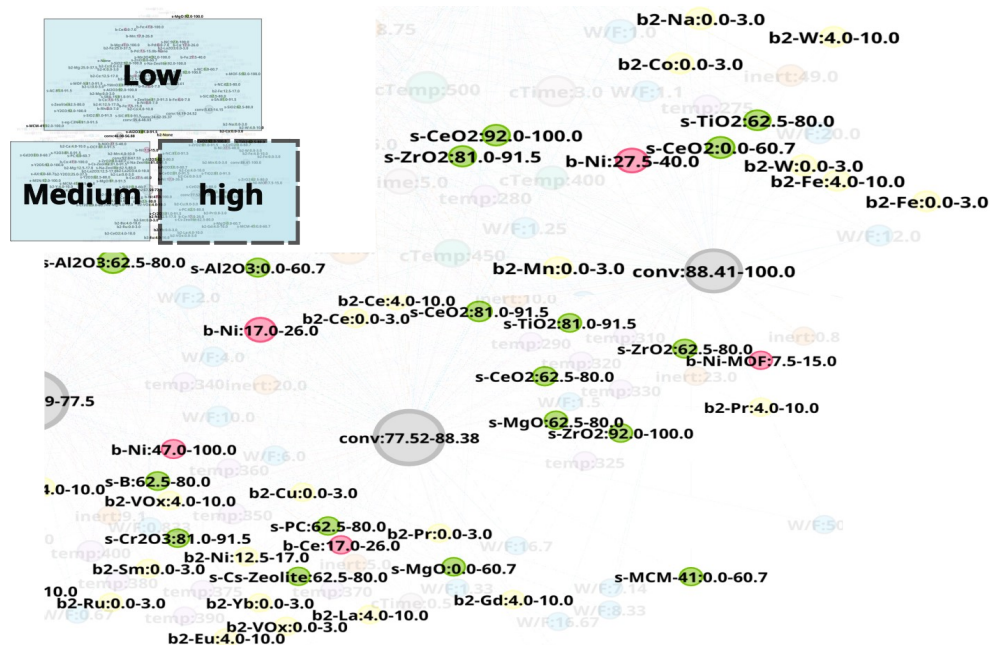


**Fig. 5** Relationship between CO<sub>2</sub> conversion(%) and catalyst elements(Base1, b<sub>1</sub>; Base2, b<sub>2</sub>; Support, s<sub>1</sub>) based on the N-1 network. High CO<sub>2</sub> conversion area is enlarged. Areas up to 35.37% is defined as low CO<sub>2</sub> conversion area, 35.4% to 77.5% is defined as medium CO<sub>2</sub> conversion area, and greater than 77.52% is defined as high CO<sub>2</sub> conversion area. Note that labels are adjusted, and node size is determined by degree ranking within a range of 10 to 40 for visualization purposes. A higher resolution of this network can be found in the support information.

chemical element combinations associated with that particular range of CO<sub>2</sub> conversion. This, therefore, makes it possible to include compatibility of each combination during analysis.

The high CO<sub>2</sub> conversion area in the N-2 network is investigated further to better understand the relationship between catalyst combinations and CO<sub>2</sub> conversion as shown in Figure 8. It can be seen that metal combinations such as NiNa, NiCo, NiFe, NiMn, NiPr, NiCe, NiVO<sub>x</sub>, NiSm, NiBa, and NiSr are associated with high CO<sub>2</sub> conversion area and are located near nodes of high CO<sub>2</sub> conversion. Elements such as Ni, Na, Co, Fe, Sm, Mn, Ce, Pr, and VO<sub>x</sub> are also included in Figure 5, while elements such as Ba and Sr seem to correlate with high CO<sub>2</sub> conversion rates when combined with Ni. In particular, the introduction of manganese into nickel-based catalysts has been demonstrated to enhance CO<sub>2</sub> conversion.<sup>33–37</sup> Furthermore, other combinations such as NiCe, NiPr, NiBa, NiFe, and NiCo, which were screened from Figure 8, have also been reported to improve CO<sub>2</sub> conversion.<sup>38–42</sup> Therefore, such catalytic networks appropriately represent the trends observed in literature data across different CO<sub>2</sub> conversion areas. Catalyst combinations associated with low CO<sub>2</sub> conversion are also examined as shown in Figure S3. In this area, combinations such as NiCo, NiCe, NiMg, and NiFe are observed. Notably, Co, Ce, and Fe also appear in the high CO<sub>2</sub> conversion area, suggesting that the apparent overlap is largely governed by the elemental composition rather than by the presence of a given element alone. As shown in Figure 8, the promoter contents in the high CO<sub>2</sub> conversion area remain limited to a few percent relative to Ni such as Ni(27.5-40.0)Co(0.0-3.0), Ni(27.5-04.0)Ce(4.0-10.0), and Ni(27.5-15.0)Fe(4.0-10.0). In contrast, Figure S3 indicates that low CO<sub>2</sub> conversion catalysts of-

ten involve comparatively excessive promoter loadings relative to Ni such as Ni(0.0–7.0)Co(12.5–17.0), Ni(0.0–7.0)Ce(12.5–17.0), and Ni(7.5–15.0)Fe(25.0–37.5). It should be noted, however, that the low CO<sub>2</sub> conversion area also includes compositions with low promoter contents such as Ni(7.5-15.0)Fe(0.0-3.0) and Ni(17.0-26.0)Co(4.0-10.0). Taken together, these observations indicate that excessive promoter addition is an unfavorable condition for achieving high CO<sub>2</sub> conversion. The network analysis reveals that certain metal combinations and compositions are systematically associated with CO<sub>2</sub> conversion. Therefore, employing these combinations and compositions may contribute to improving CO<sub>2</sub> conversion based off the trends and information present in these networks. In this study, a systematic screening of metal combinations to identify promising ternary catalysts is performed. To evaluate whether the knowledge extracted from the binary catalysts data can be extended to the design of ternary catalysts, a representative subset of screened ternary candidates (NiMnPr, NiMnCe, NiMnBa, NiMnFe, and NiMnCo) are selected. Al<sub>2</sub>O<sub>3</sub> is selected as the standard support in all catalysts for comparing the activity of element pairs.

### 3.3 Catalyst Performance

To evaluate the activity of the screened catalysts, the performance of ternary catalysts is tested at a temperature range of 150–450 °C. For comparison, CO<sub>2</sub> conversion of NiMn/Al<sub>2</sub>O<sub>3</sub>, NiCe/Al<sub>2</sub>O<sub>3</sub>, NiPr/Al<sub>2</sub>O<sub>3</sub>, and Ni/Al<sub>2</sub>O<sub>3</sub> catalysts are also examined. All three element catalysts exhibit better activity compared to Ni/Al<sub>2</sub>O<sub>3</sub>. Furthermore the effectiveness of three element catalysts become more pronounced when compared to NiMn/Al<sub>2</sub>O<sub>3</sub>. At 400 °C, the CO<sub>2</sub> conversion follows the order: NiMnCe/Al<sub>2</sub>O<sub>3</sub> (58.02 %)



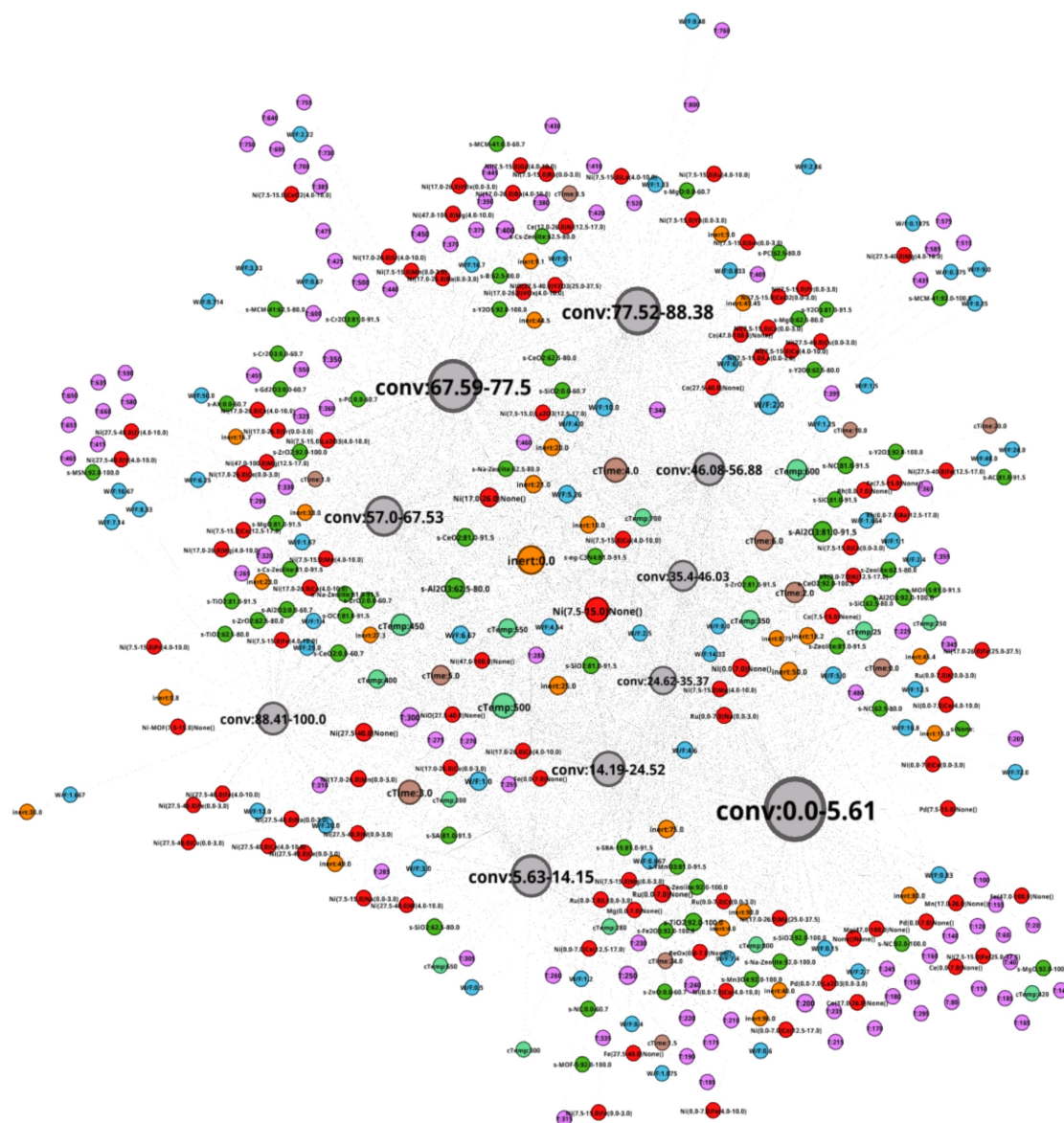


**Fig. 6** The N-2 network. Each variables is color-coded: red(catalyst), green(Support), emerald(Calcination temperature( $^{\circ}$ C)), light brown(Calcination time(h)), light purple(Temperature( $^{\circ}$ C)), light blue (W/F(mgcat/minml)), orange(Inert % in feed), and gray( $\text{CO}_2$  conversion, %). Note that labels are adjusted, and node size is determined by degree ranking within a range of 10 to 40 for visualization purposes. A higher resolution of this network can be found in the support information. A higher resolution of this network can be found in the support information.



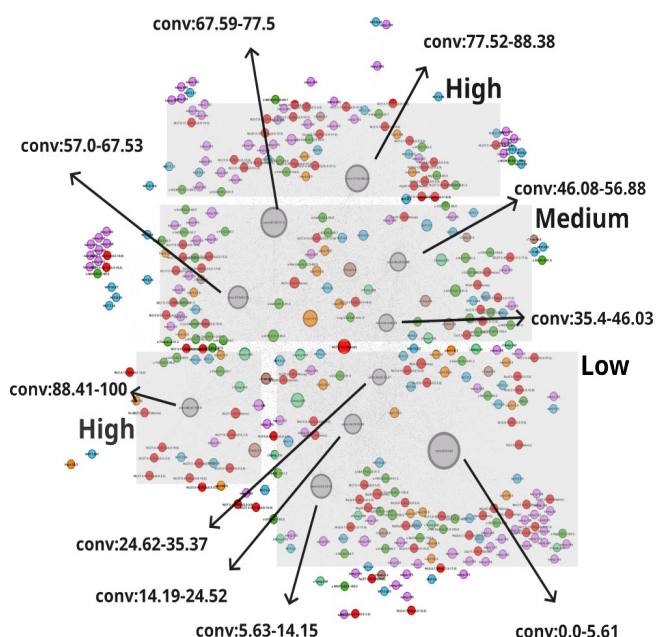


**Fig. 7** A large picture of N-2. Each variables is color-coded: red(catalyst), green(Support), emerald(Calcination temperature( $^{\circ}$ C)), light brown(Calcination time(h)), light purple(Temperature( $^{\circ}$ C)), light blue (W/F(mgcat/minml)), orange(Inert % in feed), and gray( $\text{CO}_2$  conversion, %). Areas up to 35.37 % is defined as low  $\text{CO}_2$  conversion area, 35.4 % to 77.5 % is defined as medium  $\text{CO}_2$  conversion area, and greater than 77.52 % is defined as high  $\text{CO}_2$  conversion area. A higher resolution of this network can be found in the support information.

> NiMnPr/ $\text{Al}_2\text{O}_3$  (57.33 %) > NiMnBa/ $\text{Al}_2\text{O}_3$  (49.61 %) > NiMn/ $\text{Al}_2\text{O}_3$  (48.65 %) > NiMnCo/ $\text{Al}_2\text{O}_3$  (36.70 %) > NiMnNa/ $\text{Al}_2\text{O}_3$  (31.68 %) > NiMnFe/ $\text{Al}_2\text{O}_3$  (27.99 %). The  $\text{CH}_4$  yield follows the order: NiMnPr/ $\text{Al}_2\text{O}_3$  (40.53 %) > NiMnCe/ $\text{Al}_2\text{O}_3$  (39.24 %) > NiMn/ $\text{Al}_2\text{O}_3$  (30.21 %)  $\approx$  NiMnBa/ $\text{Al}_2\text{O}_3$  (30.07 %) > NiMnCo/ $\text{Al}_2\text{O}_3$  (16.66 %) > NiMnFe/ $\text{Al}_2\text{O}_3$  (8.99 %) > NiMnNa/ $\text{Al}_2\text{O}_3$  (6.67%). Interestingly, NiMnCe/ $\text{Al}_2\text{O}_3$  and NiMnPr/ $\text{Al}_2\text{O}_3$  exhibit higher  $\text{CO}_2$  conversion than NiCe/ $\text{Al}_2\text{O}_3$  (39.22%) and NiPr/ $\text{Al}_2\text{O}_3$  (10.86%), possibly due to additional effects among the three elements, as shown in Figure9(a). Furthermore, a 12 h durability testing is conducted on NiMnPr/ $\text{Al}_2\text{O}_3$ , which exhibits the highest  $\text{CH}_4$  yield, and it demonstrated excellent stability as shown in Figure10. More detailed results for catalysts containing Ni, Mn, and/or Pr are shown in Figure S4, and a comparison with previously reported catalysts is shown in Table S1.  $\text{CO}_2$  conversion and  $\text{CH}_4$  yield of NiMnBa/ $\text{Al}_2\text{O}_3$  are comparable to those of NiMn/ $\text{Al}_2\text{O}_3$ , whereas NiMnCo/ $\text{Al}_2\text{O}_3$ , NiMnNa/ $\text{Al}_2\text{O}_3$ , and NiMnFe/ $\text{Al}_2\text{O}_3$  reduce  $\text{CO}_2$  conversion and suppress methane formation as shown in Figure9(a), (b), (d). Furthermore, as shown in Figure9(c) and (e), NiMnCe/ $\text{Al}_2\text{O}_3$ , NiMnPr/ $\text{Al}_2\text{O}_3$ , and NiMnBa/ $\text{Al}_2\text{O}_3$  can suppress CO formation, whereas NiMnCo/ $\text{Al}_2\text{O}_3$ , NiMnFe/ $\text{Al}_2\text{O}_3$ , and NiMnNa/ $\text{Al}_2\text{O}_3$  exhibit increased CO yield with rising temperature. Consequently, the activity for  $\text{CO}_2$  hydrogenation changes significantly depending on the element added to NiMn. In other words, pairing Ni-Mn with a Lanthanoid element resulted in

higher yields compared to transition (Fe, Co) and basic metals (Na, Ba). In particular, NiMnCe/ $\text{Al}_2\text{O}_3$  and NiMnPr/ $\text{Al}_2\text{O}_3$  exhibit higher  $\text{CO}_2$  conversion than corresponding binary catalysts, demonstrating their potential as promising catalysts.

### 3.4 Characterization on NiMnPr/ $\text{Al}_2\text{O}_3$

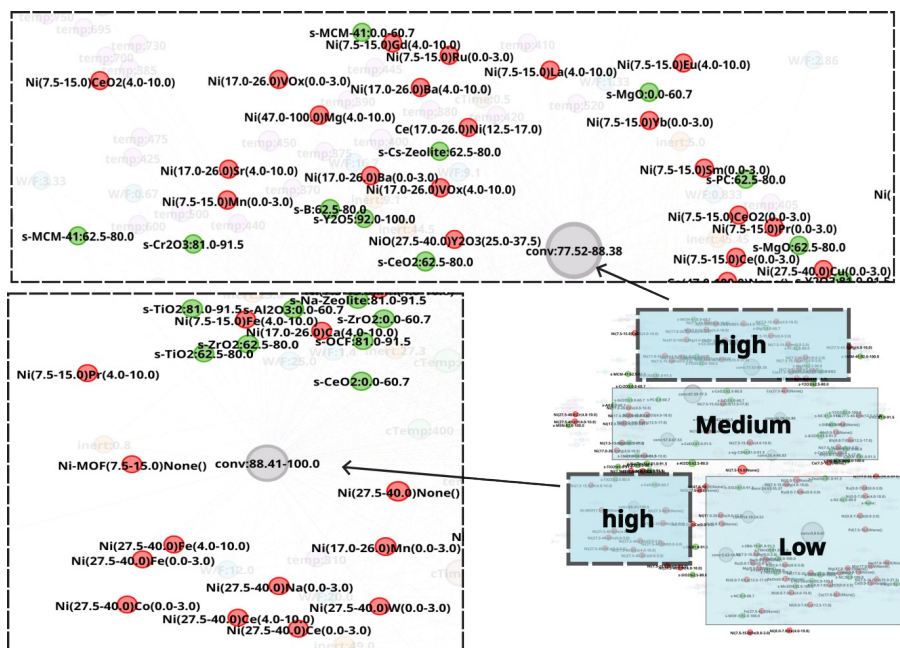
The NiMnPr/ $\text{Al}_2\text{O}_3$  catalyst, which exhibits the highest  $\text{CH}_4$  yield, is selected for detailed characterization to identify the physico-chemical features responsible for its superior performance. XRD is investigated to confirm the crystal structure. The XRD patterns of catalysts containing Ni, Mn, and/or Pr are shown in Figure11(a), while those of the other catalysts are provided in Figure S5. As shown in Figure11(a), XRD patterns show the characteristic diffraction peaks of  $\gamma$ -alumina, whereas no peaks corresponding to the Ni, Mn, and Pr are detected. The absence of peaks indicates that either the concentration of the crystalline phase of the species containing the impregnated elements is very low or they are not forming crystalline phases. Furthermore, no differences in peak intensity or shift are observed among catalysts.

SEM-EDS analyses is conducted to confirm morphology and surface compositions of the synthesized catalysts. As shown in Figure11(b), although no peaks related to Mn, Ni, or Pr are observed in XRD, SEM-EDS confirms the presence of these three elements. The catalyst appears as an agglomeration with an average diameter of approximately 5  $\mu\text{m}$ . SEM-EDS elemental mapping confirms the presence of Ni, Mn and Pr on the  $\gamma$ - $\text{Al}_2\text{O}_3$  support. The Ni-K, Mn-K and Pr-L maps show broadly distributed signals over the observed area indicating good dispersion at the micrometer scale. SEM-EDS for other catalysts also shows in Figure S6-S8.

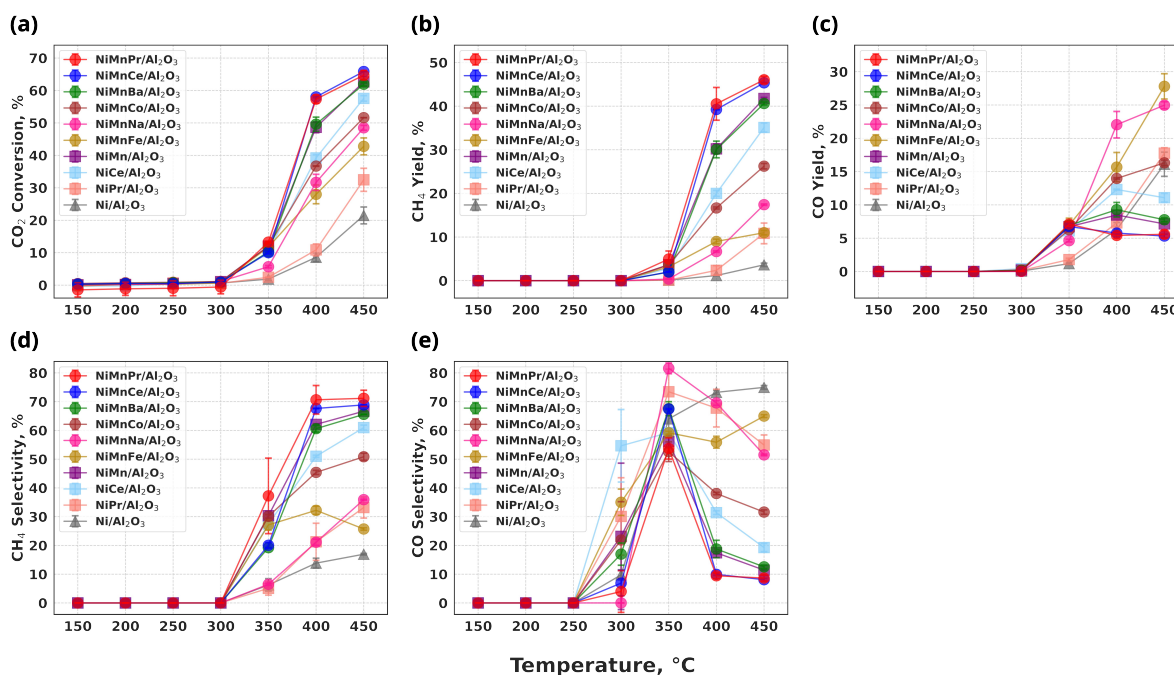
$\text{CO}_2$  adsorption-desorption measurements are performed to investigate the  $\text{CO}_2$  related properties of the catalysts. As shown in Figure11(c), the  $\text{CO}_2$  uptake is in the order of Pr/ $\text{Al}_2\text{O}_3$ , Ni/ $\text{Al}_2\text{O}_3$ , Mn/ $\text{Al}_2\text{O}_3$  for the unary catalysts. NiPr/ $\text{Al}_2\text{O}_3$  exhibits the highest  $\text{CO}_2$  uptake, followed by NiMnPr/ $\text{Al}_2\text{O}_3$  with a nearly comparable value, and then by MnPr/ $\text{Al}_2\text{O}_3$  and Pr/ $\text{Al}_2\text{O}_3$ , whereas other Pr-free catalysts have relatively lower  $\text{CO}_2$  uptake. It is considered that Pr-containing catalyst systems enhance  $\text{CO}_2$  adsorption and activation.<sup>43</sup> In other words, the addition of Pr to Ni or Ni-Mn catalysts increases  $\text{CO}_2$  uptake. This result is consistent with the higher  $\text{CO}_2$  conversion and  $\text{CH}_4$  yield observed for the NiMnPr and NiPr catalysts compared with the NiMn and Ni catalysts at 400 $^{\circ}$ C, as shown in Figure 9(a) and (b). Therefore, the Pr in the ternary catalyst may also contribute to changes in surface properties related to  $\text{CO}_2$ .

The results of  $\text{H}_2$ -TPR profile are shown in Figure11(d). Ni/ $\text{Al}_2\text{O}_3$  indicates a large reduction peak at 600  $^{\circ}$ C from 300  $^{\circ}$ C to 800  $^{\circ}$ C, attributed to the reduction of NiO to Ni metal. Mn/ $\text{Al}_2\text{O}_3$  gives broad peak at around 150-500  $^{\circ}$ C, derived from sequential reduction steps of Mn oxides such as  $\text{MnO}_2$  to  $\text{Mn}_2\text{O}_3$ ,  $\text{Mn}_3\text{O}_4$  and MnO. Pr/ $\text{Al}_2\text{O}_3$  does not serve any obvious reduction profile below 900  $^{\circ}$ C. The addition of Pr to Mn or Ni slightly increases the shoulder peak area at lower temperature, which is likely due to an increase in the number of easily reduced Mn or Ni species. There are significant differences in binary NiMn and ternary NiMnPr catalysts in comparison to unary Ni and Mn

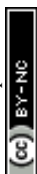




**Fig. 8** Details of high CO<sub>2</sub> conversion area in the N-2 network. Catalyst (pink), Support (green), and CO<sub>2</sub> conversion (gray) are highlighted. Note that labels are adjusted, and node size is determined by degree ranking within a range of 10 to 40 for visualization purposes. A higher resolution of this network can be found in the support information.



**Fig. 9** (a) CO<sub>2</sub> conversion, %, (b) CH<sub>4</sub> yield, %, (c) CO yield, %, (d) CH<sub>4</sub> selectivity, %, and (e) CO selectivity, % as a function of temperature. Ternary, binary, and unary catalysts are represented by circles, squares, and triangles, respectively. Note that the plots and error bars at each temperature represent the average and standard deviation of two measurements to ensure reproducibility.



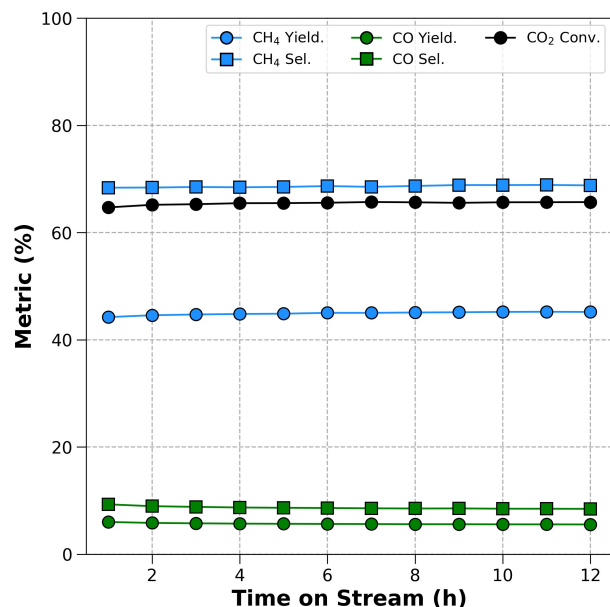


Fig. 10 A 12 h durability test for NiMnPr/Al<sub>2</sub>O<sub>3</sub> at 450° under H<sub>2</sub>/CO<sub>2</sub> of 4.

catalysts. Both NiMn and NiMnPr catalysts possess two-humped reduction peak. It is considered that the lower temperature profile at 100–350 °C from MnO<sub>2</sub> into Mn<sub>2</sub>O<sub>3</sub> and Mn<sub>2</sub>O<sub>3</sub> into MnO whereas the higher temperature profile 350–750 °C from NiO into Ni origin, respectively.<sup>36</sup> It is very interesting that the peak at higher temperature derived from Ni origin gives gradual shift to the lower temperature at the top peak from 585 °C (NiAl<sub>2</sub>O<sub>3</sub>), 530 °C (NiMnAl<sub>2</sub>O<sub>3</sub>) to 475 °C (NiMnPrAl<sub>2</sub>O<sub>3</sub>). The improved reducibility of NiO contributes to the fine dispersion of the as-generated Ni. As the result, higher catalytic activity is observed in the binary NiMn/Al<sub>2</sub>O<sub>3</sub> systems in earlier studies.<sup>44,45</sup> This trend is consistent with the enhanced CO<sub>2</sub> conversion and CH<sub>4</sub> yield observed for these catalysts as shown in Figure 9(a) and (b). Overall, considering CO<sub>2</sub> uptake and H<sub>2</sub>-TPR profile, the unique NiMnPr catalyst, which is experimentally validated as facilitating CO<sub>2</sub> methanation at lower temperatures, clearly indicates the effect of additive Pr for further improvement of NiMn nature.

## 4 Conclusions

CO<sub>2</sub> hydrogenation dataset is utilized to structure multidimensional data via network analysis. The constructed network provides insights into which experimental conditions are effective or not for the catalysts data across multidimensional variables. Furthermore, the networks are applied to catalyst screening, identifying useful catalyst combinations. Six ternary element catalysts selected from high CO<sub>2</sub> conversion area are developed and experimentally validated. NiMnPr/Al<sub>2</sub>O<sub>3</sub> and NiMnCe/Al<sub>2</sub>O<sub>3</sub> demonstrate activity exceeding that of their respective binary element catalysts. This result demonstrates that network-based trends and knowledge can efficiently discover new catalysts. This approach not only uncovers key trends and relationships across multidimensional variables in complex heterogeneous reactions but also establishes a generalizable strategy for guiding the design of ef-

ficient catalysts. These findings highlight the potential of data-driven network methodologies to accelerate catalyst discovery and provide a framework for exploring complex catalytic systems.

## 5 Support Information

- Source dataset(xlsx), support information(pdf), high-resolution Figure1(png), and high-resolution Figure6(png)
- Raw chromatograms and calculated catalyst activities from activity test

## 6 Acknowledgment

This work is funded by the Japan Science and Technology Agency (JST) ERATO grant number (JPMJER1903), PRESTO grant number (JPMJPR24T5), and JST Mirai Program Grant Number (JPMJMI25G1), JSPS KAKENHI Grant-in-Aid for Scientific Research (B) Grant Number (JP23H01762) and (24K01241). This work is also supported by the research fund "Hokkaido University-Hitachi Joint Cooperative Support Program for Education and Research".

## Notes and references

- 1 Junaedi, C.; Hawley, K.; Walsh, D.; Roychoudhury, S.; Abney, M.; Perry, J. Compact and lightweight sabatier reactor for carbon dioxide reduction. 41st International Conference on Environmental Systems. 2011; p 5033.
- 2 Romegialli, S.; Tripodi, A.; Gramegna, A.; Tommasi, M.; Ramis, G.; Rossetti, I. Production of Synthetic Methane for Aerospace Applications: A Mars Case. *Industrial & Engineering Chemistry Research* **2024**, *64*, 190–208.
- 3 Ghaib, K.; Nitz, K.; Ben-Fares, F.-Z. Chemical methanation of CO<sub>2</sub>: A review. *ChemBioEng Reviews* **2016**, *3*, 266–275.
- 4 Tommasi, M.; Degerli, S. N.; Ramis, G.; Rossetti, I. Advances in CO<sub>2</sub> methanation: A comprehensive review of catalysis, reactor design and process optimization. *Chemical Engineering Research and Design* **2024**, *201*, 457–482.
- 5 Liu, G.; Sun, S.; Sun, H.; Zhang, Y.; Lv, J.; Wang, Y.; Zeng, J.; Yan, Z.; Wu, C. Integrated CO<sub>2</sub> capture and utilisation: A promising step contributing to carbon neutrality. *Carbon Capture Science & Technology* **2023**, *7*, 100116.
- 6 Lee, W. J.; Li, C.; Prajitno, H.; Yoo, J.; Patel, J.; Yang, Y.; Lim, S. Recent trend in thermal catalytic low temperature CO<sub>2</sub> methanation: A critical review. *Catalysis today* **2021**, *368*, 2–19.
- 7 Fan, W. K.; Tahir, M. Recent trends in developments of active metals and heterogenous materials for catalytic CO<sub>2</sub> hydrogenation to renewable methane: A review. *Journal of environmental chemical engineering* **2021**, *9*, 105460.
- 8 Rui, N.; Zhang, X.; Zhang, F.; Liu, Z.; Cao, X.; Xie, Z.; Zou, R.; Senanayake, S. D.; Yang, Y.; Rodriguez, J. A.; others Highly active Ni/CeO<sub>2</sub> catalyst for CO<sub>2</sub> methanation: Preparation and characterization. *Applied Catalysis B: Environmental* **2021**, *282*, 119581.
- 9 Sun, H.; Lv, J.; Wang, C.; Zhang, Y.; Sun, S.; Zhang, P.; Cheng, G.; Mei, D.; Wang, Y.; Yan, Z. Ru/CeO<sub>2</sub> catalysts with enriched oxygen vacancies by plasma treatment for efficient CO<sub>2</sub> methanation. *Fuel* **2025**, *381*, 133413.



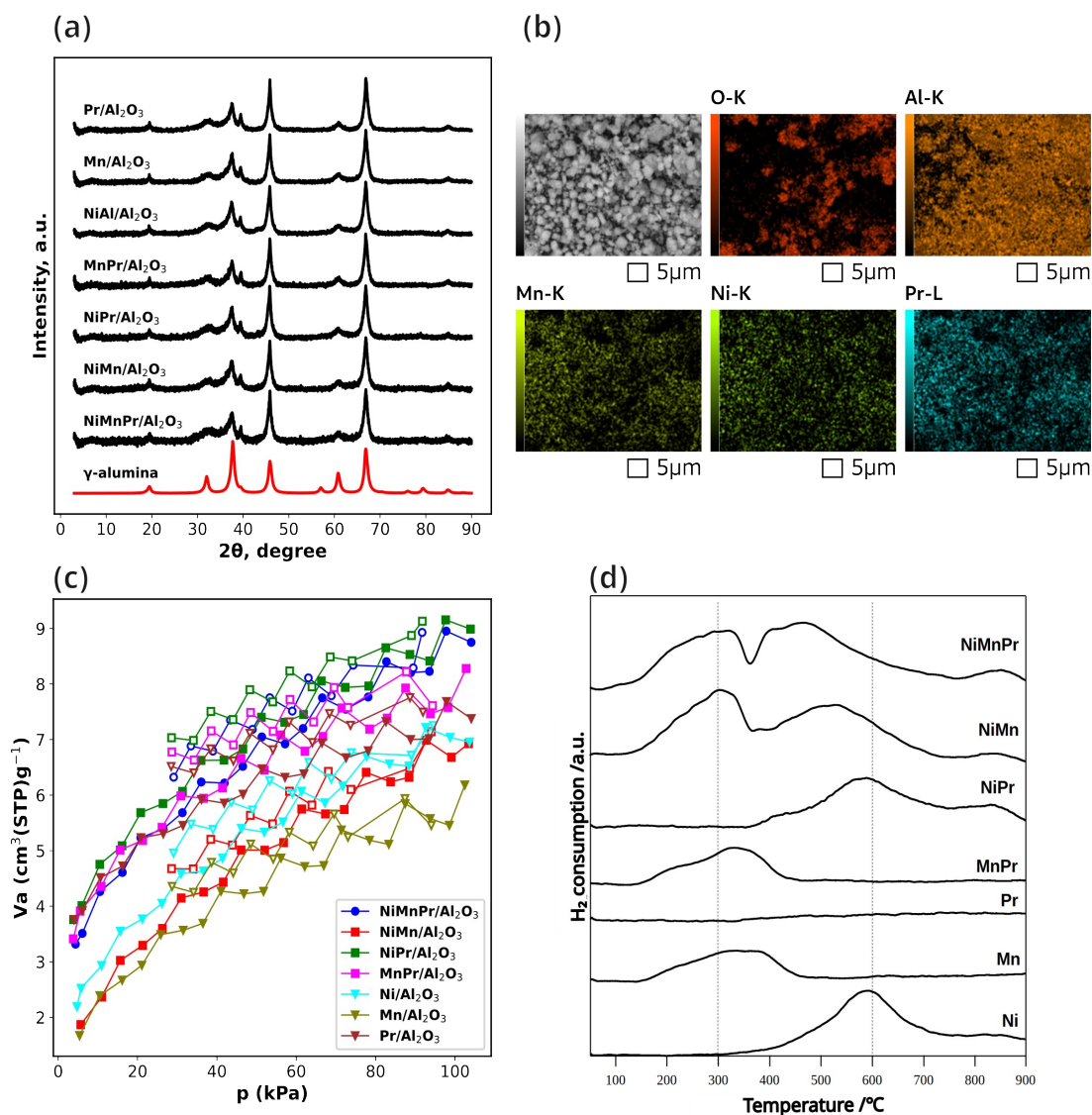
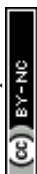
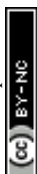


**Fig. 11** (a) XRD for catalysts with Ni, Pr, or Mn. The reference pattern shown in red is obtained from the built-in database of the Rigaku Miniflex 600-C software. (b) The SEM-EDS image for NiMnPr/Al<sub>2</sub>O<sub>3</sub>. (c) CO<sub>2</sub> adsorption and desorption for catalysts with Ni, Pr, or Mn. (d) H<sub>2</sub>-TPR profiling for catalysts with Ni, Pr, or Mn.



- 10 Kuhaudomlap, S.; Srifa, A.; Koo-Amornpattana, W.; Fukuhara, C.; Ratchahat, S. Insight and comprehensive study of Ni-based catalysts supported on various metal oxides for CO<sub>2</sub> methanation. *Scientific Reports* **2024**, *14*, 23149.
- 11 Shen, L.; Xu, J.; Zhu, M.; Han, Y. Essential role of the support for nickel-based CO<sub>2</sub> methanation catalysts, *ACS Catal.* **10** (2020) 14581–14591.
- 12 Tada, S.; Jinushizono, T.; Ishikawa, K.; Miyazaki, S.; Toyao, T.; Shimizu, K.-i.; Nishijima, M.; Yamauchi, N.; Kobayashi, Y.; Kikuchi, R. Low-temperature CO<sub>2</sub> methanation over Ru nanoparticles supported on monoclinic zirconia. *Energy & Fuels* **2024**, *38*, 2296–2304.
- 13 Quindimil, A.; De-La-Torre, U.; Pereda-Ayo, B.; Davó-Quñonero, A.; Bailón-García, E.; Lozano-Castello, D.; González-Marcos, J. A.; Bueno-López, A.; González-Velasco, J. R. Effect of metal loading on the CO<sub>2</sub> methanation: A comparison between alumina supported Ni and Ru catalysts. *Catalysis Today* **2020**, *356*, 419–432.
- 14 Younas, M.; Loong Kong, L.; Bashir, M. J.; Nadeem, H.; Shehzad, A.; Sethupathi, S. Recent advancements, fundamental challenges, and opportunities in catalytic methanation of CO<sub>2</sub>. *Energy & Fuels* **2016**, *30*, 8815–8831.
- 15 Medina, O. E.; Amell, A. A.; López, D.; Santamaría, A. Comprehensive review of nickel-based catalysts advancements for CO<sub>2</sub> methanation. *Renewable and Sustainable Energy Reviews* **2025**, *207*, 114926.
- 16 Molinet-Chinaglia, C.; Shafiq, S.; Serp, P. Low temperature sabatier CO<sub>2</sub> methanation. *ChemCatChem* **2024**, *16*, e202401213.
- 17 Ahmad, F.; Lovell, E. C.; Masood, H.; Cullen, P. J.; Ostrikov, K. K.; Scott, J. A.; Amal, R. Low-temperature CO<sub>2</sub> methanation: synergistic effects in plasma-Ni hybrid catalytic system. *ACS Sustainable Chemistry & Engineering* **2020**, *8*, 1888–1898.
- 18 Wei, C.; Ding, H.; Zhang, Z.; Lin, F.; Xu, Y.; Pan, W. Research progress of bimetallic catalysts for CO<sub>2</sub> hydrogenation to methane. *International Journal of Hydrogen Energy* **2024**, *58*, 872–891.
- 19 Shi, J. On the synergetic catalytic effect in heterogeneous nanocomposite catalysts. *Chemical reviews* **2013**, *113*, 2139–2181.
- 20 Vojvodic, A.; Nørskov, J. K. New design paradigm for heterogeneous catalysts. *National Science Review* **2015**, *2*, 140–143.
- 21 Toyao, T.; Maeno, Z.; Takakusagi, S.; Kamachi, T.; Takigawa, I.; Shimizu, K.-i. Machine learning for catalysis informatics: recent applications and prospects. *Acs Catalysis* **2019**, *10*, 2260–2297.
- 22 Takahashi, K.; Ohyama, J.; Nishimura, S.; Fujima, J.; Takahashi, L.; Uno, T.; Taniike, T. Catalysts informatics: paradigm shift towards data-driven catalyst design. *Chemical Communications* **2023**, *59*, 2222–2238.
- 23 Takahashi, K.; Takahashi, L.; Le, S. D.; Kinoshita, T.; Nishimura, S.; Ohyama, J. Synthesis of heterogeneous catalysts in catalyst informatics to bridge experiment and high-throughput calculation. *Journal of the American Chemical Society* **2022**, *144*, 15735–15744.
- 24 Benavides-Hernandez, J.; Dumeignil, F. From characterization to discovery: Artificial intelligence, machine learning and high-throughput experiments for heterogeneous catalyst design. *ACS Catalysis* **2024**, *14*, 11749–11779.
- 25 Garcia-Escobar, F.; Takahashi, L.; Shaaban, A.; Nishimura, S.; Takahashi, K. Design of low temperature La<sub>2</sub>O<sub>3</sub> oxidative coupling of methane catalysts using feature engineering and automated sampling. *Catalysis Science & Technology* **2025**, *15*, 92–99.
- 26 Yilmaz, B.; Oral, B.; Yıldırım, R. Machine learning analysis of catalytic CO<sub>2</sub> methanation. *International Journal of Hydrogen Energy* **2023**, *48*, 24904–24914.
- 27 Rudin, C. Stop explaining black box machine learning models for high stakes decisions and use interpretable models instead. *Nature machine intelligence* **2019**, *1*, 206–215.
- 28 Hasukawa, Y.; Garcia-Escobar, F.; Takahashi, K.; Takahashi, L. Multidimensional Catalysis Data Representation for Designing Oxidative Coupling of Methane Catalysts. *The Journal of Physical Chemistry C* **2024**, *129*, 391–401.
- 29 Takahashi, L.; Yamada, T.; Okamoto, H.; Takahashi, K. Unveiling the relation between multiple chemical products and process conditions for trichloroethylene and perchloroethylene production via catalysis network analysis. *Catalysis Science & Technology* **2024**, *14*, 4927–4938.
- 30 Takahashi, L.; Nguyen, T. N.; Nakanowatari, S.; Fujiwara, A.; Taniike, T.; Takahashi, K. Constructing catalyst knowledge networks from catalyst big data in oxidative coupling of methane for designing catalysts. *Chemical Science* **2021**, *12*, 12546–12555.
- 31 Jacomy, M.; Venturini, T.; Heymann, S.; Bastian, M. ForceAtlas2, a continuous graph layout algorithm for handy network visualization designed for the Gephi software. *PLoS one* **2014**, *9*, e98679.
- 32 Bastian, M.; Heymann, S.; Jacomy, M. Gephi: an open source software for exploring and manipulating networks. *Proceedings of the international AAAI conference on web and social media*. 2009; p 361–362.
- 33 Vrijburg, W. L.; Moiola, E.; Chen, W.; Zhang, M.; Terlingen, B. J.; Zijlstra, B.; Filot, I. A.; Züttel, A.; Pidko, E. A.; Hensen, E. J. Efficient base-metal NiMn/TiO<sub>2</sub> catalyst for CO<sub>2</sub> methanation. *Acs Catalysis* **2019**, *9*, 7823–7839.
- 34 Qiang, D.; Mei, T.; Liu, Y.; Ye, Z.; Li, Z.; Zhao, S. High-Performance NiMn-LDO Catalysts for Efficient CO<sub>2</sub> Methanation. *Langmuir* **2025**,
- 35 Qiang, D.; Mei, T.; Liu, Y.; Jin, H.; Ye, Z.; Li, Z.; Zhao, S. Enhanced low-temperature activity for CO<sub>2</sub> methanation over N-doped NiMn-LDO. *Chemical Engineering Journal* **2025**, *507*, 160839.
- 36 Zhang, W.; Xu, L.; Zhou, F.; Sun, F.; Xu, J.; Zhu, M.; others Manganese-promoted Ni/Al<sub>2</sub>O<sub>3</sub> catalysts for effective CO<sub>2</sub> methanation. *Journal of Catalysis* **2025**, *448*, 116215.
- 37 Burger, T.; Koschany, F.; Thomys, O.; Köhler, K.; Hinrichsen, O. CO<sub>2</sub> methanation over Fe- and Mn-promoted co-



- precipitated Ni-Al catalysts: Synthesis, characterization and catalysis study. *Applied Catalysis A: General* **2018**, *558*, 44–54.
- 38 Wang, W.; Chu, W.; Wang, N.; Yang, W.; Jiang, C. Mesoporous nickel catalyst supported on multi-walled carbon nanotubes for carbon dioxide methanation. *international journal of hydrogen energy* **2016**, *41*, 967–975.
- 39 Ahmad, W.; Younis, M. N.; Shawabkeh, R.; Ahmed, S. Synthesis of lanthanide series (La, Ce, Pr, Eu & Gd) promoted Ni/ $\gamma$ -Al<sub>2</sub>O<sub>3</sub> catalysts for methanation of CO<sub>2</sub> at low temperature under atmospheric pressure. *Catalysis Communications* **2017**, *100*, 121–126.
- 40 Liang, C.; Hu, X.; Wei, T.; Jia, P.; Zhang, Z.; Dong, D.; Zhang, S.; Liu, Q.; Hu, G. Methanation of CO<sub>2</sub> over Ni/Al<sub>2</sub>O<sub>3</sub> modified with alkaline earth metals: Impacts of oxygen vacancies on catalytic activity. *international journal of hydrogen energy* **2019**, *44*, 8197–8213.
- 41 Pandey, D.; Deo, G. Effect of support on the catalytic activity of supported Ni–Fe catalysts for the CO<sub>2</sub> methanation reaction. *Journal of Industrial and Engineering Chemistry* **2016**, *33*, 99–107.
- 42 Alrafei, B.; Polaert, I.; Ledoux, A.; Azzolina-Jury, F. Remarkably stable and efficient Ni and Ni-Co catalysts for CO<sub>2</sub> methanation. *Catalysis Today* **2020**, *346*, 23–33.
- 43 Ju, Y.; Bae, D.; Park, J.; Choi, H. W.; Kang, J.; Ryu, K.-H.; Kim, Y. J.; Kim, M.; Kang, S. B. Role of electronic modulation of Ni-Pr bimetallic catalyst for low-temperature CO<sub>2</sub> methanation. *Applied Catalysis B: Environment and Energy* **2025**, *379*, 125675.
- 44 Le, T. A.; Kim, J.; Kang, J. K.; Park, E. D. Co and CO<sub>2</sub> methanation over m (mmn, ce, zr, mg, k, zn, or v)-promoted Ni/Al<sub>2</sub>O<sub>3</sub> catalysts. *Catalysis Today* **2020**, *348*, 80–88.
- 45 Huang, L.; Zhang, F.; Chen, R.; Hsu, A. T. Manganese-promoted nickel/alumina catalysts for hydrogen production via auto-thermal reforming of ethanol. *International journal of hydrogen energy* **2012**, *37*, 15908–15913.



All data is provided in the manuscript/

